Nano Research
2019, 12(2): 449–455

ISSN 1998-0124 CN 11-5974/O4
https://doi.org/10.1007/s12274-018-2238-y

Research Article

Plasmon-tunable Au@Ag core-shell spiky nanoparticles for surface-enhanced Raman scattering

Zhulin Huang[1], Guowen Meng[1,2] (✉), Xiaoye Hu[1], Qijun Pan[1,2], Dexian Huo[1,2], Hongjian Zhou[1], Yan Ke[1], and Nianqiang Wu[3] (✉)

[1] *Key Laboratory of Materials Physics and Anhui Key Laboratory of Nanomaterials and Technology, Institute of Solid State Physics, Chinese Academy of Sciences, P. O. Box 1129, Hefei 230031, China*
[2] *University of Science and Technology of China, Hefei 230026, China*
[3] *Department of Mechanical and Aerospace Engineering, West Virginia University, P.O. Box 6106, Morgantown, WV 26506, USA*

Received: 13 September 2018 / **Revised:** 20 October 2018 / **Accepted:** 30 October 2018

ABSTRACT

A facile synthetic approach has been developed to prepare uniform and size-tunable spiky Au@Ag core-shell nanoparticles (NPs) to tailor the localized surface plasmon resonance (LSPR) properties. The gradual assembly of small Au nanocrystals allows the size of spiky Au NPs to be modulated from tens to several hundreds of nanometers by tuning the concentration of initial Au seeds and Au source; and the thickness of the Ag shell can be adjusted with stepwise reduction of Ag(I) ions. The LSPR bands of such spiky Au@Ag core-shell NPs resemble those of pure spiky Au NP cores of similar sizes in near-infrared region, and increasing the Ag shell thickness results in a blue shift and broadening of the LSPR band in the near-infrared region. Additionally, the spiky Au@Ag core-shell NPs exhibit improved surface-enhanced Raman scattering (SERS) activity as compared to the bare spiky Au NPs and spherical Ag@Au NPs. This work has offered a facile route to synthesize plasmonic metal NPs with LSPR band in 650 to 800 nm that show strong enhancement of localized electromagnetic field, which provides an effective SERS substrate for SERS imaging and detection in biological fluids and tissues.

KEYWORDS

localized surface plasmon resonance, gold, silver, surface-enhanced Raman spectroscopy

1 Introduction

Plasmonic nanoparticles (NPs) find extensive applications in cell imaging [1], thermal therapy [2, 3], nanophotonics [4], plasmon-induced photocatalysis [5–8], plasmon-enhanced signal amplification such as surface-enhanced Raman scattering (SERS) [9–12], and fluorescence [13, 14]. Various synthetic strategies have been developed to control the shape, size, and surface property of Au and Ag NPs. To date, research drives gradually from simple spheres to complex shaped and hierarchical NPs [15–17], such as nanorods [18], triangular nanoplates [19, 20], cubes [21, 22], polyhedrons [23, 24], and spiky NPs [25, 26], and further to plasmonic assemblies so that the plasmonic properties of NPs can be tailored [27]. Tuning the localized surface plasmon resonance (LSPR) band of Au and Ag NPs to the biological optical window or therapeutic window in the near-infrared (NIR) wavelength range from 650 to 1,350 nm is of particular interest to biological imaging and detection. In particular, SERS for detection and imaging in biological fluids and tissue typically uses the excitation laser of 785 nm, which demands the LSPR band to be controlled in the range around 650 to 800 nm to allow the resonance enhancement of SERS. Therefore it is significant to develop plasmonic metal NPs with LSPR band in 650 to 800 nm that show strong enhancement of localized electromagnetic (EM) field [10].

To meet the above-mentioned need of SERS imaging and detection in biological fluids and tissues, stellate or spiky NPs characterized by multiple sharp spikes receive the attention of researcher because they exhibit strong antenna enhancement effect (LSPR effect) from visible to NIR spectral region [28–32]. According to the previous study, the core of spiky Au NPs serves as a nanoscale antenna for the surrounding spikes while enhancing the localized electromagnetic fields at the tip surface [25]. The highest SERS enhancement factors for molecules adsorbed near the tips of Au nanostar could reach 10 orders of magnitude [26], depending on the sharpness of Au tips. Researchers are interested in spiky Au NPs due to the good chemical stability, biocompatibility and easy surface functionalization. Currently researchers are making efforts to further improve the EM enhancement factors (EFs) of Au NPs with LSPR band in the NIR spectral range. This drives researchers to look at Ag NPs because Ag NPs show stronger EM enhancement and higher plasmonic efficiency than Au NPs [33]. However, it is difficult to tune the LSPR band of Ag NPs to the NIR region; and it is challenging to synthesize spiky Ag NPs because of the fast diffusion rate of Ag atoms during the liquid phase synthesis process.

Based on the above considerations, we herein synthesize the spiky Au@Ag core-shell nanoparticles, which are expected to show stronger EM enhancement than that of the bare spiky Au NPs; and the LSPR band can be further tuned by the Ag shell [34–36]. In fact, Samal et al. have reported the synthesis of Au@Ag core-shell nanospheres [35]. The results have revealed that the core-shell NPs demonstrate improved SERS performance under the varied excitation wavelengths. Nevertheless, no systematic study of spiky Au@Ag core-shell NPs with controlled Ag shell thickness has been demonstrated. In this study, a facile approach is devised to prepare the spiky Au@Ag core-shell NPs with tunable Au core size and Ag shell thickness for SERS-based detection application, as shown in Scheme 1. In this synthetic process, the spiky Au NPs are prepared and stabilized in

Address correspondence to Guowen Meng, gwmeng@issp.ac.cn; Nianqiang Wu, nick.Wu@mail.wvu.edu

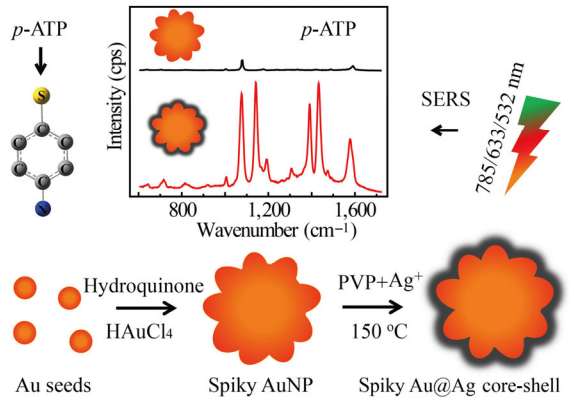

Scheme 1 Schematic illustration of the preparation process of the spiky Au@Ag core-shell NPs.

water without the frequently used surfactants such as cetyltrimethylammonium bromide and polymers. Hydroquinone is utilized as the reducing agent instead of traditional citrate because of the higher redox potential negativity versus the normal hydrogen electrode, enabling the immediate formation of Au atoms at room temperature [37]. The Au atoms then nucleate and assemble on the Au seeds, which grow rapidly but anisotropically to yield the spiky Au NPs. Especially, we will optimize the synthetic parameters, such as the concentrations of Au seeds, hydroquinone, and Au source to control the full width at half maxima of LSPR bands from 550 to 820 nm. Furthermore, a layer of Ag shell is uniformly deposited on the spiky Au NPs according to a polyol process. The thickness of the Ag shell can be precisely tailored from 2 to 10 nm by adjusting the concentration of Ag precursor.

2 Experimental

2.1 Materials

Chloroauric acid ($HAuCl_4{\cdot}4H_2O$), silver nitrate ($AgNO_3$), trisodium citrate, hydroquinone, *para*-aminothiophenyl (*p*-ATP) and ethanol were bought from Sinopharm Chemical Reagent limited corporation. Poly(vinyl pyrrolidone) (PVP-K29, $(C_6H_9NO)_n$, M_W = 58,000), 1,5-pentanediol, and thiram were obtained from Aladdin. Milli-Q deionized (DI) water (resistivity = 18.2 MΩ/cm) was used for all preparations.

2.2 Synthesis of spiky Au NPs

Spiky Au NPs were prepared by Au seed mediated method. The 13 nm sized Au nanospheres were first prepared by reducing chloroauric acid (200 μL, 100 mg/mL) with trisodium citrate (5 mL, 20 mg/mL) in a round flask containing 45 mL of DI water under continuous stirring (400 rpm). The flask was kept above 90 °C in an oil bath. Then, portion of the as-prepared suspensions (0.1–4.0 mL) was injected into a round flask containing water (30 mL) and $HAuCl_4{\cdot}4H_2O$ (100 μL, 100 mg/mL). Fresh aqueous solution of hydroquinone (2 mL, 10 mg/mL) was then quickly injected into the mixture. The reaction proceeded at room temperature with mild stirring (300 rpm). Within five minutes, the color of the solution changed from opaque to pink, then purple/blue for small spiky Au NPs, and finally deep blue and even green for large spiky Au NPs. The product was washed by centrifugation-redispersion for two cycles, and finally dispersed in ethanol. All the molarity concentrations could be established according to the equivalent weights.

2.3 Synthesis of spiky Au@Ag core-shell NPs

The Ag shell was *in-situ* deposited on the previous spiky Au NPs through a polyol process at 150 °C. Pentanediol solution of PVP-K29 (16 mg/mL) and $AgNO_3$ (10 mg/mL) were prepared respectively. All the as-prepared spiky Au NPs were re-dispersed in pentanediol (1 mL), ultrasonicated, and shaken up for 50 min at 1,500 rpm by a vortex. Subsequently, pentanediol (5 mL), PVP solution (1 mL), and spiky Au NPs were injected in a round flask and heated to 150 °C with an oil bath. In this process, the mixture was stirred continuously at 400 rpm. Pentanediol solution of $AgNO_3$ (0.1–1 mL, containing 1–10 mg $AgNO_3$) was then injected into the mixture. After 40 min, the reaction was terminated. The solution containing spiky Au@Ag core-shell NPs were naturally cooled down and separated by centrifugation-redispersion for twice and dispersed in ethanol. Herein, the thickness of Ag the shell was tuned by applying different volumes of $AgNO_3$ precursor. Again, all the molarity concentrations could be established according to the equivalent weights.

2.4 Synthesis of spherical Au@Ag core-shell NPs

Firstly, Au nanospheres with diameter larger than 13 nm were synthesized similar to the case of spiky Au NPs. By using a higher concentration of Au seeds (4 mL), $HAuCl_4$ (40 mg), and hydroquinone (80 mg), 80 nm sized Au nanospheres can be synthesized. The product was then washed, dispersed in 1,5-pentadenial and further coated with Ag shell by the method similar to the case of preparing spiky Au@Ag core-shell NPs.

2.5 Characterization

The morphology and composition of NPs were examined using scanning electron microscope (SEM, Hitachi SU8020) and transmission electron microscope (TEM, JEOL 2010), which were both equipped with energy dispersive X-ray spectrometer (EDS). A multi-functional X-ray diffractometer (X'Pert Pro MPD, Philips) was used to evaluate the crystallinity. The optical absorption spectra of the products were measured by an ultraviolet–visible–near-infrared (UV–Vis–NIR) spectrophotometer (Varian, Cary 500).

2.6 Raman measurement

All Raman spectra were recorded by a confocal microprobe Raman spectrometer (Renishaw Invia, 532, 633, and 785 nm laser line, 50× objective). The laser power was 1% for 532 nm excitation (~ 0.3 mW), 10% for 633 excitation (~ 0.51 mW), and 1% for 785 nm excitation (~ 0.75 mW). The accumulation time was 1 s unless stated. The obtained SERS signals at varied excitation wavelengths were normalized for comparison. To improve the distribution uniformity of nanoparticles on Si wafer, each Si substrate was firstly immersed in piranha solution to expose the surface –OH groups, and then in aminopropyltriethoxysilane (APTES) ethanol solution (10 mg/mL) for 30 min to obtain abundant $-NH_2$ groups near the Si surface. Such handled Si substrates were then immersed in nanoparticle suspensions to load the particles through electrostatic force attraction [38]. The Si substrates with evenly distributed nanoparticles were then cast with analyte solutions of varied concentrations but the same amount (5 μL), and naturally dried. Each SERS spectrum was averaged from at least five measurements.

2.7 Simulation

The electric field distributions of the spiky NPs were simulated with finite element modeling (FEM) method using a Comsol Multiphysics 3.5a software. Model parameters were based on the observed microstructures. Optical constants of Au and Ag were adopted from the literature, in corresponding to an incident wavelength of 785 nm [39].

3 Results and discussion

3.1 Effects of the concentration of Au seeds

Figure 1 shows the morphologies of spiky Au NPs. Generally, the

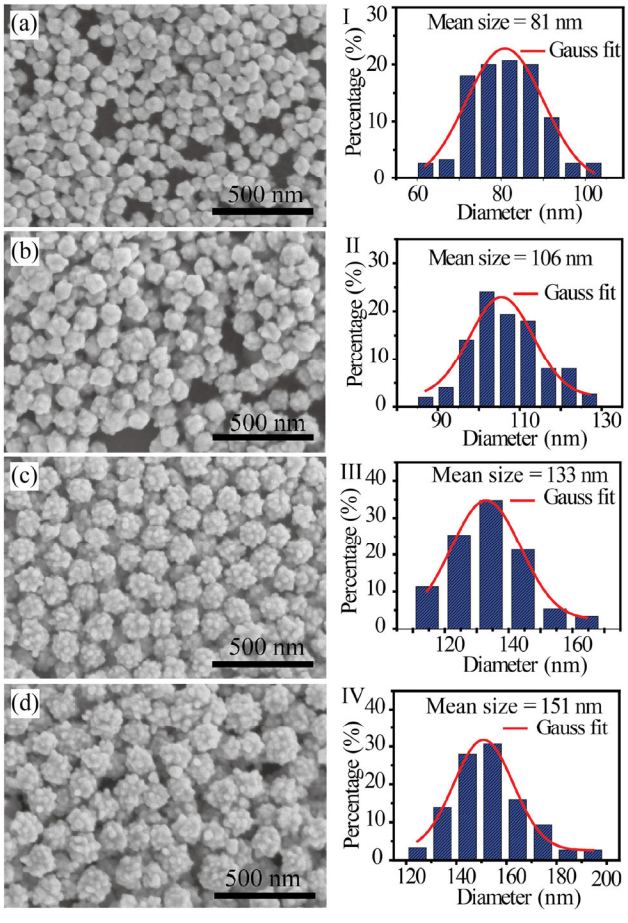

Figure 1 (a)–(d) SEM images of spiky Au NPs with varied amount Au seeds of 1.0, 0.4, 0.2, and 0.1 mL, resulting in different particle sizes as shown in the right column from Plot I to Plot IV, respectively.

spiky Au NPs showed mono-dispersity; and the yield reached 99%. Meanwhile, the product can be always reproduced from batch to batch. By simply tuning the initial concentration of small Au seeds and maintaining the content of hydroquinone (20 mg) and $HAuCl_4{\cdot}4H_2O$ (10 mg), the spiky Au NPs with varied diameters can be readily obtained. Typically, a large amount of Au seeds tended to yield small spiky Au NPs (about 81, Fig. 1(a) and the size distribution plot I in the right column), whereas a small amount of Au seeds simply yielded larger spiky Au NPs with more spikes (Fig. 1(d) and size distribution plot IV in the right column). The size of spiky Au NPs can be tuned from 81 to 151 nm by varying Au seed amount (1.0, 0.4, 0.2, and 0.1 mL), as shown in Fig. 1. Spontaneously, the number of protruding spikes increased from 10–15 (the 81 nm sample) to 25–30 (the 151 nm sample). The size variation was due to the different contents of Au source in the solution contributed to each small Au seeds. Obviously at a lower Au seed concentration, the particles can be fully developed. If too much Au seeds (4 mL) were added, the Au nanospheres would simply grow larger instead of forming obviously protruding spikes (Fig. S1 in the Electronic Supplementary Material (ESM)). This was due to the limited Au source but excessive Au seeds in precursor solution, which hindered the further growth of Au NPs. Also, the number density of spikes changed in this process. Assume that the spiky Au NPs form a hexagonal closely-packed monofilm. Then $\rho_N = nS/(2\sqrt{3}r^2)$, where ρ_N is the number density of spikes, n is the number of spikes on each single Au NP, S is the unit area, r is the radius of spiky Au NP. In this way, the proportion of ρ_N between the 81 nm sample and 151 nm sample is $\rho_{N81}:\rho_{N151} = n_{81}r_{151}^2:n_{151}r_{81}^2 = 1.6:1$. In this sense, the number density of spikes decreased a little as the spiky Au NPs grow larger.

Actually, the presented SEM images reveal that the spiky shape indeed gradually evolved. This was further confirmed by the corresponding TEM images in Figs. 2(a)–2(c). It was observed that the spikes grew longer with increasing the NP size, from 5–10 nm (81 nm sample), 10–15 nm (106 nm sample), 13–17 nm (133 nm sample), to 15–20 nm for the 151 nm sample. By subtracting the length of protruding spikes, the general core size thus became 66, 81, 103, and 116 nm, respectively. The growth mechanism was similar to what we reported previously [37], in which small Fe_3O_4 NPs were used as seeds. Herein the small Au nanospheres were used as the seeds instead. The spiky shape can be similarly considered to result from the self-assembly of individual small Au NPs into larger ones around the Au seeds. Initially, upon addition of hydroquinone, numerous monocrystalline Au NPs were generated (Fig. 2(d)) in the solution. Meanwhile, the Au atoms would settle on the larger Au seeds used initially (Fig. 2(e)), which were finally evolved into larger fringes (Fig. 2(f)) and retained single-crystalline. The free small Au NPs spontaneously interacted with the larger Au seeds and grew larger due to the Ostwald ripening effect. As such, the spiky NPs could be fully grown into larger ones until exhaustion of the small Au NPs and the Au atoms. Nevertheless, the dark field image and selected area electron diffraction (SAED) pattern of all the spiky Au NP suggested poly-crystallinity (Figs. 2(g)–2(i)).

3.2 Effects of hydroquinone concentration

The concentration of reducing agent also affects the morphology of final product. Generally in the chemical reaction, a hydroquinone molecule evolves into benzoquinone by providing two electrons through the equation: 3 Hydroquinone + 2 Au^{3+} = 3 Benzoquinone + 6 H^+ + 2 Au^0. So a theoretical mole ratio of M[hydroquinone]: M[$AuCl_4^-$] larger than 3:2 should be sufficient to reduce all the Au precursor. Herein, 10 mg of $HAuCl_4{\cdot}4H_2O$ and 1 mL of Au seeds were injected in 30 mL of DI water. Various amounts of hydroquinone (5, 10, 20, and 40 mg) were injected in the reaction solution, respectively. From the SEM observations (Fig. S2 in the ESM), the size of spiky Au NPs becomes slightly smaller when increasing the hydroquinone concentration, but the overall size didn't change much. Nevertheless at an obviously higher concentration of reducing agent, small Au nanocrystals of even higher particle density are formed quickly. On one hand, the small Au crystals assembled on the Au seeds and formed small spiky Au NPs. On the other hand, some of the small spiky Au NPs together with the small Au crystals were evolved into spherical micro/nano structure following the Ostwald ripening effect (Fig. S2(d) in the ESM). Each Au micro/nano structure demonstrated small protrusions on the surface.

3.3 Effect of $HAuCl_4$ concentration

The concentration of initial $HAuCl_4$ is very important to the size and morphology of the final product. As mentioned above, with a constant concentration of Au seeds (200 μL) and excessive reducing agent (20 mg hydroquinone) but different content of $HAuCl_4$ precursor, one can directly monitor the morphological evolution of spiky Au NPs and elucidate the growth mechanism of the spiky Au NPs. In this case, the $HAuCl_4$ precursor solutions containing 1, 2, 5, 10, 15, and 20 mg of $HAuCl_4{\cdot}4H_2O$ were applied respectively. SEM characterization indicated that with 1 mg of $HAuCl_4{\cdot}4H_2O$ addition, the Au seeds simply grew into larger ones with a few particles assembled together. With more $AuCl_4^-$ ions participated in the reaction, the nanoparticles obviously grew larger, the well-defined spikes then appeared. The particle finally developed larger due to the excessive smaller particles ready for self-assembly (Fig. S3 in the ESM). At this stage, the spiky Au NPs seemed more like roughed spheres due to the over growth (Fig. S3(f) in the ESM).

3.4 SERS activity of the spiky Au NPs

The optical absorption bands of the spiky Au NPs (liquid-phase) in Fig. 3(a) clearly showed a size-dependent relationship. The spiky Au NPs exhibited the LSPR band from 522 to 707 nm, and the full width at half maxima of LSPR can be extended to 820 nm. The 133 nm sized spiky Au NPs with LSPR band at 678 nm were examined by 532, 633, and 785 nm excitations using the "non-resonant" *p*-ATP as the probe molecules. The results in Fig. 3(b) indicated strong vibrational bands of *p*-ATP under excitation wavelengths of 633 nm and 785 nm. At 532 nm excitation, only the 1,080 cm^{-1} shift (C–S stretching) and 1,591 cm^{-1} shift (phenyl ring stretching) can be observed. This can be ascribed to the fact that the LSPR band of 133 nm spiky Au NPs centered at 678 nm was partially overlapped with the wavelengths of both the 785 and 633 nm laser sources, which in turn excited the LSPR effect of spiky Au NPs for higher electric field enhancement. To be emphasized, when the NPs were assembled on substrates for SERS measurements (Fig. S4 in the ESM), the surrounding media and the aggregating state of NPs changed, leading to a broaden and slightly red shifted plasmon band closer to 785 nm excitation (Fig. S5 in the ESM). Thus the 785 nm excitation leaded to higher SERS intensities compared to the case of 633 nm. On the other hand, the LSPR bands of spiky Au NPs would gradually blue shift with a decrease in the particle size. In this manner, the relatively larger spiky Au NPs showed distinctly larger enhancement at 785 nm laser excitation (Fig. 3(c)), due to the fact that LSPR bands of the 133 and 151 nm sized Au nanoparticles had more overlap with the wavelength of excitation laser. However, the 133 nm sized Au NPs showed higher SERS enhancement effect than that of the 151 nm sized counterparts (the upper two curves in Fig. 3(c)) because the former had more sharp tips on the surface (Figs. 1(c) and 1(d)). This was further proved by the FEM simulations (Fig. S6 in the ESM).

3.5 Spiky Au@Ag core-shell NPs

Subsequently, the as-prepared spiky Au NPs were used as the "templates" to prepare the spiky Au@Ag core-shell NPs with a

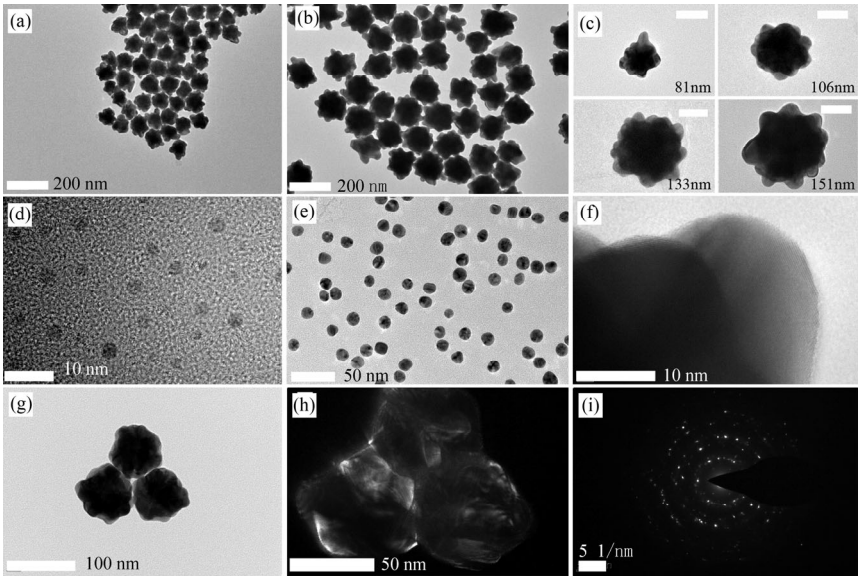

Figure 2 TEM images of spiky Au NPs with mean size of 81 nm (a) and 151 nm (b), and individual spiky Au NPs with gradually developed size (c), all scale bars indicate 50 nm. TEM images of small Au crystals in the product (d), 13 nm Au seeds (e), and the single-crystalline fringes with clear lattice patterns on a 151 nm spiky Au NP (f). Bright field TEM image of the 81 nm spiky Au NP trimer (g), the dark field counterpart (h), and the corresponding SAED patterns of all the spiky Au NP (i), showing polycrystalline feature.

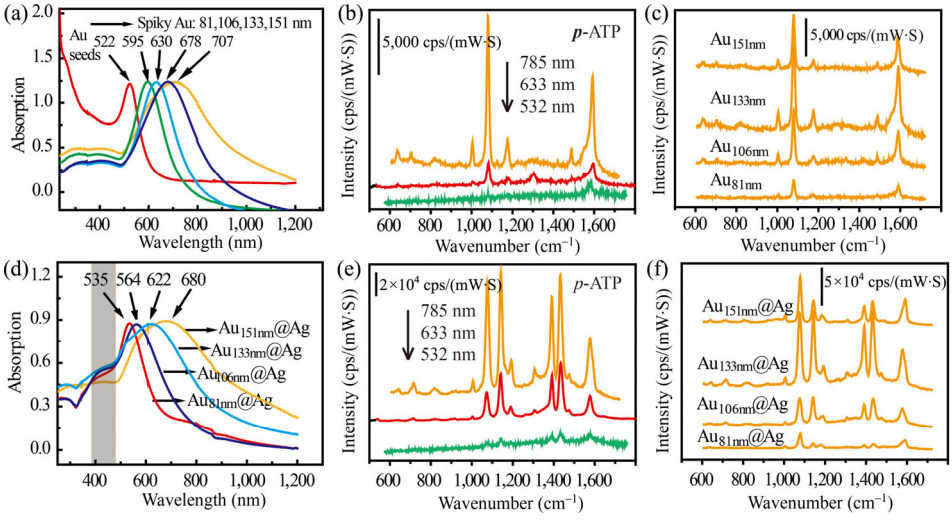

Figure 3 (a) UV–Vis–NIR absorption spectra of spiky Au NPs with varied sizes in their solution phase. (b) SERS spectra of *p*-ATP adsorbed on the 133 nm spiky Au NPs measured under different excitation sources. (c) Comparative SERS spectra of *p*-ATP adsorbed on spiky Au NPs with varied mean sizes. (d) UV–Vis–NIR absorption spectra of spiky Au@Ag core-shell NPs. (e) SERS spectra of *p*-ATP adsorbed on the spiky $Au_{133nm}@Ag_{2nm}$ NPs measured under different excitation sources. (f) Comparative SERS spectra of *p*-ATP adsorbed on spiky Au NPs with varied sizes but identical $AgNO_3$ precursor (2 mg).

polyol protocol developed by Xia, et al. [15]. Briefly, silver ions were reduced *in-situ* on the spiky Au NPs. The size of spiky Au NPs and the concentration of Ag^+ can be tuned to achieve an optimal morphology, and more details can be found in the experimental section. Upon adding 2 mg of $AgNO_3$ precursor in the reaction solution, the final products showed distinct color change (Fig. S7 in the ESM) and a blue shift of the LSPR band (Fig. 3(d)) compared to that of the spiky Au NPs in Fig. 3(a). The LSPR band at around 420 nm was originated from the Ag shell, as indicated by the dashed area in Fig. 3(d). It is noted that the Ag layer thickness herein for the four different sized spiky Au NPs was slightly varied but approximately the same (see the explanations in the ESM). The typical thickness of Ag shell was about 2 nm (Figs. 4(a)–4(c)) for the 133 nm sample. In this case, the spiky morphology was well maintained. Meanwhile, the thickness of Ag shell increased by increasing the mass of $AgNO_3$ precursor. For example, addition of 5 mg of $AgNO_3$ precursor into the reaction solution resulted in a 6 nm thick Ag shell on the spiky Au NPs (Figs. 4(d)–4(f)). If too much $AgNO_3$ precursor (10 mg) was injected, very thick Ag shell would grow on the surface of the Au NPs. In this case, the spikes gradually disappeared (Figs. 4(g) and 4(h)) as more Ag atoms isotropically accumulated on the particle surface. Finally, the shell distributed unevenly around Au surface. The typical thickness of Ag shell would exceed 10 nm at the concave region between neighboring spikes. Furthermore, the EDS spectra in Fig. 4(i) showed that the Ag shell thickness increased with an increased Ag content ratio.

3.6 SERS enhancement of the spiky Au@Ag core-shell NPs

The SERS activity of the core-shell NPs was evaluated using *p*-ATP as the probe molecules. Taking the spiky $Au_{133nm}@Ag_{2nm}$ sample as an example, the relative peak intensities of ν_{C-S} at 1,080 cm^{-1} shift increased by about 6.5 times under excitation of the 785 nm laser, 6 times for the 633 nm laser excitation and 4.5 times for the 532 nm laser excitation (Fig. 3(e)). These comparative results were based on the same amount of analyte solution (5 μL) dispersed on both types of substrates. It was seen that some new peaks appeared at 1,142, 1,193, 1,390, and 1,432 cm^{-1} in the presence of Ag. These new vibrational modes were due to the diazotization of two amine groups, which was catalyzed by the strong and matching plasmons of Au@Ag core-shell NPs [40]. In addition, comparative SERS measurement in Fig. 3(f) demonstrated that the SERS enhancement was improved for all the four samples with varied Au NP size but the same Ag precursor (2 mg). Meanwhile, we compared the SERS sensitivity between Au@Ag core-shell nanospheres (Fig. S8 in the ESM, 80 nm Au core and ~ 2 nm Ag shell) and spiky Au@Ag core-shell NPs (81 nm spiky Au core and 2 nm Ag shell), as shown by Fig. S9 in the ESM. Obviously, both samples showed strong vibrational bands of *p*-ATP, but the spiky ones demonstrated 2–3 times higher SERS intensity.

The LSPR of spiky Au@Ag core-shell NPs was sensitive to the thickness of the Ag shell. Figure 5(a) shows that the LSPR peak of NPs shifts from 680 to 565 nm when the Ag shell thickness increased to 3 nm. Meanwhile, as the Ag shell thickness increased, the core-shell NPs gradually exhibited broad and red-shifted LSPR band, which resulted in stronger coupling between the excitation source and the plasmon of the core-shell NPs. As the Ag shell further increased, the spikes tended to evolve as smooth protrusions, leading to weak LSPR. This explains why the SERS efficiency (shown in Fig. 5(b)) of thin-shelled (2 and 3 nm) samples were high but became much weaker for thick-shelled counterparts, as further testified by the FEM simulations in Fig. S10 in the ESM.

The improvement of the SERS enhancement by the spiky Au@Ag core-shell NPs with 2–3 nm Ag shell can be ascribed to the following reasons: i) Ag has stronger plasmon than Au for the identical

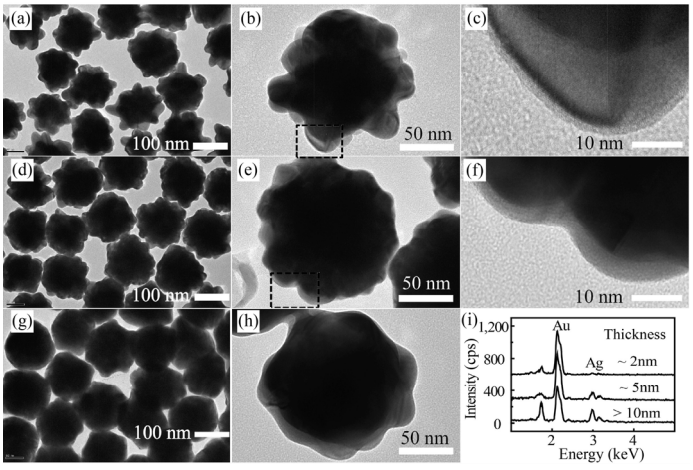

Figure 4 (a) and (b) TEM images of spiky Au@Ag core-shell NPs achieved by adding 2 mg $AgNO_3$ as the Ag source. (c) Close-up view showing the ~2 nm Ag shell. (d) and (e) TEM images of spiky Au@Ag core-shell NPs achieved by adding 5 mg $AgNO_3$ as the Ag source. (f) Close-up view showing the ~6 nm Ag shell. (g) TEM images of spiky Au@Ag core-shell NPs prepared by adding 10 mg $AgNO_3$. (h) Close-up view showing the thick Ag shell over 10 nm. (i) EDS spectra of spiky Au@Ag core-shell NPs with varied Ag shell thicknesses.

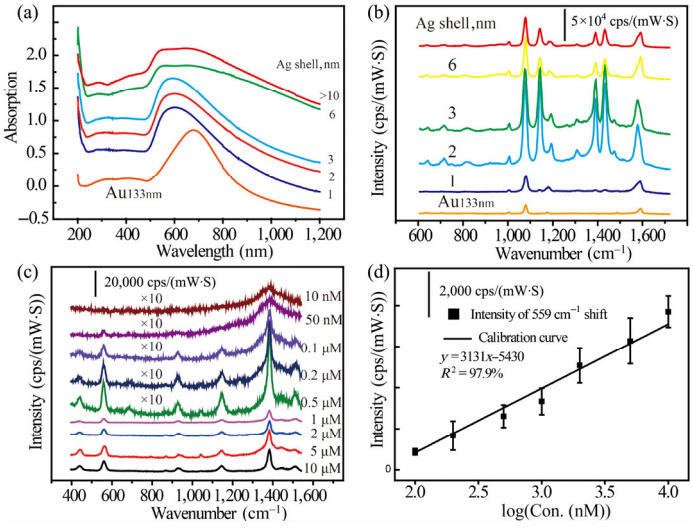

Figure 5 (a) UV–Vis–NIR absorption spectra of spiky Au@Ag core-shell NPs with different Ag shell thicknesses. (b) SERS spectra of *p*-ATP (10 μM) adsorbed on the spiky Au@Ag core-shell NPs with varied Ag shell thicknesses. (c) SERS spectra of thiram with varied concentrations adsorbed on spiky $Au_{133nm}@Ag_{2nm}$ core-shell NPs. (d) Averaged relative intensities (from 12 measurements) of the 559 cm^{-1} mode as a function of logarithmic concentration of thiram. The calibration curve shows a linear range from 0.1 to 10 μM.

structure [33], thus the coating of Ag shell on the Au core leads to strong LSPR and EM enhancement, as evidenced by the simulation results in Figs. S6 and S10 in the ESM; ii) the original roughness of each spike from core-shell NPs was not affected by coating of such a thin shell (Fig. S10 in the ESM); iii) the blue shifted but broad LSPR band from the core-shell NPs contributed to stronger coupling between the excitation wavelength and the LSPR of NPs. The LSPR herein also became broad, making the 633 and 785 nm are still in partial resonance with the blue shifted LSPR. In this way, EM enhancement is still high.

The average SERS EFs of the spiky Au and Au@Ag core-shell NPs were estimated by comparing the normalized SERS intensity and the Raman intensity, using the formula $EF = (I_{SERS}/N_{SERS})(I_{RS}/N_{RS})^{-1}$ [41]. More details of the calculation of enhancement factor can be found in the ESM, in which *p*-ATP was used as a standard probe molecule to evaluate the enhancement. Under the excitation of

785 nm excitation, the average EF value was 1.2×10^6 for spiky Au_{133nm} NPs and 6.7×10^7 for spiky $Au_{133nm}@Ag_{2nm}$ core-shell NPs.

Specially, the spiky $Au_{133nm}@Ag_{2nm}$ core-shell NPs were used for detection of environmental pollutants, such as thiram, a widely used plant fungicide. Recently, thiram has been reported to be added into bean sprout to retain the freshness, which enters the food chain. Herein, ethanol solution of thiram with various concentrations were cast on the spiky Au@Ag core-shell NPs substrates and dried, and excited by the 785 nm laser. The SERS spectra in Fig. 5(c) displayed seven prominent vibrational fingerprints of thiram molecules at varied concentrations. According to the calculations by Gaussian 03W software at B3LYP/6-31 G(d) level, the vibrational assignments of thiram were summarized as follows: 438 cm^{-1} (C–N scissoring), 559 cm^{-1} (C–N scissoring), 927 cm^{-1} (C=S stretching), 1,145 cm^{-1} (C=N stretching), 1,380 cm^{-1} (C–H wagging), 1,440 cm^{-1} (C–H twisting), and 1,507 cm^{-1} shift (C–N stretching). When the concentration decreased to 50 nM, only the strong peak at 559 cm^{-1} can be discriminated. According to our linear fit plot of peak intensity (559 cm^{-1} shift) versus the logarithmic concentration of thiram in Fig. 5(d), the limit of detection of thiram was calculated to be 70 nM for the spiky Au@Ag core-shell NPs, which was defined as the concentration at the signal-to-noise ratio of 3 [42].

Also, the SERS signal stability of spiky Au@Ag core-shell NPs was investigated. The first issue was to verify the SERS signal reproducibility of such a substrate. Repeated Raman measurements on thirty different sites of the substrate indicated that the relative signal deviation of the 559 cm^{-1} shift of thiram was 19.5% (Fig. S11 in the ESM). The other issue was to investigate the stability of spiky Au@Ag core-shell NPs as Ag-based nanostructures would lose SERS sensitivity easily due to the active surfaces [43]. It was demonstrated that the signal intensity of the 559 cm^{-1} shift decreased by 40% within 6 months (Fig. S12 in the ESM), which may be resulted from the oxidation of Ag surface.

To investigate the real SERS detection applications by the spiky core-shell NPs, the residual solution of fresh bean sprout (bought from a local supermarket) was examined by SERS spectroscopy. As shown by Fig. S14 in the ESM, one sample (6 g) was stored in ethanol (15 mL) for 8 h, the other sample was immersed in thiram (10^{-4} M) for 8 h and taken out and stored in ethanol again. Obviously demonstrated by the optical images, the thiram treated bean sprouts showed better freshness. It is shown that the purchased bean sprout do not show any fingerprints of thiram while the thiram treated sample can be discriminated according to the 554 cm^{-1} shift (C–N scissoring) and 1,370 cm^{-1} shift (C–H wagging). Furthermore, these two modes were verified to come from the enhanced Raman signals of thiram pollution rather than the pure thiram. This is because at such concentration (10^{-4} M) and measuring conditions, the normal Raman signals of thiram could not be obtained (the bottom curve of Fig. S14(b) in the ESM).

4 Conclusions

In summary, a synthetic approach was developed to grow the spiky Au@Ag core-shell NPs with controlled Au core size and Ag shell thickness. The Ag shell was *in-situ* deposited on the surface of the spiky Au NPs with the shell thickness in a range of 2–10 nm. The LSPR band of the spiky Au@Ag core-shell NPs can be tuned to the near-infrared region, depending on the particle size. The plasmonic band of Au@Ag core-shell NPs, which resembled those of the bare spiky Au NP cores of similar sizes, showed a blue shift, and was broadened upon coating with the Ag shell. In particular, the spiky Au@Ag core-shell NPs showed 55 times higher SERS sensitivity than that of the bare Au counterpart under excitation of the 785 nm laser. The spiky Au@Ag core-shell NPs have a great potential in SERS imaging and detection in biological fluids and tissues.

Acknowledgements

This work was financially supported by the National Basic Research Program of China (No. 2013CB934304), Key Research Program of Frontier Sciences, CAS (No. QYZDJ-SSW-SLH046), the CAS/SAFEA International Partnership Program for Creative Research Teams, the Natural Science Foundation of China (Nos. 21673245, 51632009, 51628202, 51472245 and 51671186), Hefei Institutes of Physical Sciences, CAS, and the Youth Innovation Promotion Association of CAS.

Electronic Supplementary Material: Supplementary material (SEM images, TEM images, SERS spectra and FEM simulation results of the spiky and core-shell spiky nanostructures, optical images of the suspensions of spiky NPs, optical absorbance spectra of the SERS substrates) is available in the online version of this article at https://doi.org/10.1007/s12274-018-2238-y.

References

[1] Lee, K. S.; El-Sayed, M. A. Gold and silver nanoparticles in sensing and imaging: Sensitivity of Plasmon response to size, shape, and metal composition. *J. Phys. Chem. B* **2006**, *110*, 19220–19225.

[2] Jain, P. K.; Huang, X. H.; El-Sayed, I. H.; El-Sayed. M. A. Noble metals on the nanoscale: Optical and photothermal properties and some applications in imaging, sensing, biology, and medicine. *Acc. Chem. Res.* **2008**, *41*, 1578–1586.

[3] Huang, P.; Pandoli, O.; Wang, X. S.; Wang, Z.; Li, Z. M.; Zhang, C. L.; Chen, F.; Lin, J.; Cui, D. X.; Chen, X. Y. Chiral guanosine 5′-monophosphate-capped gold nanoflowers: Controllable synthesis, characterization, surface-enhanced Raman scattering activity, cellular imaging and photothermal therapy. *Nano Res.* **2012**, *5*, 630–639.

[4] Ozbay, E. Plasmonics: Merging photonics and electronics at nanoscale dimensions. *Science* **2006**, *311*, 189–193.

[5] Hao, C. L.; Xu, L. G.; Ma, W.; Wu, X. L.; Wang, L. B.; Kuang, H.; Xu, C. L. Unusual circularly polarized photocatalytic activity in nanogapped gold-silver chiroplasmonic nanostructures. *Adv. Funct. Mater.* **2015**, *25*, 5816–5822.

[6] Wu, N. Q. Plasmonic metal-semiconductor photocatalysts and photoelectrochemical cells: A review. *Nanoscale* **2018**, *10*, 2679–2696.

[7] Hou, W. B.; Cronin, S. B. A review of surface Plasmon resonance-enhanced photocatalysis. *Adv. Funct. Mater.* **2013**, *23*, 1612–1619.

[8] Collins, G.; Holmes, J. D. Engineering metallic nanoparticles for enhancing and probing catalytic reactions. *Adv. Mater.* **2016**, *28*, 5689–5695.

[9] Yang, S. K.; Lapsley, M. I.; Cao, B. Q.; Zhao, C. L.; Zhao, Y. H.; Hao, Q. Z.; Kiraly, B.; Scott, J.; Li, W. Z.; Wang, L. et al. Large-scale fabrication of three-dimensional surface patterns using template-defined electrochemical deposition. *Adv. Funct. Mater.* **2013**, *23*, 720–730.

[10] Li, M.; Cushing, S. K.; Wu, N. Q. Plasmon-enhanced optical sensors: A review. *Analyst* **2015**, *140*, 386–406.

[11] Rodríguez-Lorenzo, L.; Álvarez-Puebla, R. A.; Pastoriza-Santos, I.; Mazzucco, S.; Stéphan, O.; Kociak, M.; Liz-Marzán, L. M.; Javier Garcia de Abajo, F. Zeptomol detection through controlled ultrasensitive surface-enhanced Raman scattering. *J. Am. Chem. Soc.* **2009**, *131*, 4616–4618.

[12] Prikhozhdenko, E. S.; Bratashov, D. N.; Gorin, D. A.; Yashchenok, A. M. Flexible surface-enhanced Raman scattering-active substrates based on nanofibrous membranes. *Nano Res.* **2018**, *11*, 4468–4488.

[13] Langguth, L.; Punj, D.; Wenger, J.; Koenderink, A. F. Plasmonic band structure controls single-molecule fluorescence. *ACS Nano* **2013**, *7*, 8840–8848.

[14] Tao, A. R.; Habas, S.; Yang, P. D. Shape control of colloidal metal nanocrystals. *Small* **2008**, *4*, 310–325.

[15] Xia, Y. N.; Xiong, Y. J.; Lim, B.; Skrabalak, S. E. Shape-controlled synthesis of metal nanocrystals: Simple chemistry meets complex physics? *Angew. Chem., Int. Ed.* **2008**, *48*, 60–103.

[16] Yang, S. K.; Lei, Y. Recent progress on surface pattern fabrications based on monolayer colloidal crystal templates and related applications. *Nanoscale* **2011**, *3*, 2768–2782.

[17] Hamon, C.; Liz-Marzán, L. M. Hierarchical assembly of plasmonic nanoparticles. *Chem. Eur.–J.* **2015**, *21*, 9956–9963.

[18] Jana, N. R.; Gearheart, L.; Murphy, C. J. Wet chemical synthesis of high aspect ratio cylindrical gold nanorods. *J. Phys. Chem. B* **2001**, *105*, 4065–4067.
[19] Chen, L.; Ji, F.; Xu, Y.; He, L.; Mi, Y. F.; Bao, F.; Sun, B. Q.; Zhang, X. H.; Zhang, Q. High-yield seedless synthesis of triangular gold nanoplates through oxidative etching. *Nano Lett.* **2014**, *14*, 7201–7206.
[20] Qian, H. M.; Xu, M.; Li, X. W.; Ji, M. W.; Cheng, L.; Shoaib, A.; Liu, J. J.; Jiang, L.; Zhu, H. S.; Zhang, J. T. Surface micro/nanostructure evolution of Au-Ag alloy nanoplates: Synthesis, simulation, plasmonic photothermal and surface-enhanced Raman scattering applications. *Nano Res.* **2016**, *9*, 876–885.
[21] Yang, Y.; Liu, J. Y.; Fu, Z. W.; Qin, D. Galvanic replacement-free deposition of Au on Ag for core-shell nanocubes with enhanced chemical stability and SERS activity. *J. Am. Chem. Soc.* **2014**, *136*, 8153–8156.
[22] Ruditskiy, A.; Xia, Y. N. Toward the synthesis of sub-15 nm Ag nanocubes with sharp corners and edges: The roles of heterogeneous nucleation and surface capping. *J. Am. Chem. Soc.* **2016**, *138*, 3161–3167.
[23] Henzie, J.; Grünwald, M.; Widmer-Cooper, A.; Geissler, P. L.; Yang, P. D. Self-assembly of uniform polyhedral silver nanocrystals into densest packings and exotic superlattices. *Nat. Mater.* **2012**, *11*, 131–137.
[24] Henzie, J.; Andrews, S. C.; Ling, X. Y.; Li, Z. Y.; Yang, P. D. Oriented assembly of polyhedral plasmonic nanoparticle clusters. *Proc. Natl. Acad. Sci. USA* **2013**, *110*, 6640–6645.
[25] Hao, F.; Nehl, C. L.; Hafner, J. H.; Nordlander, P. Plasmon resonances of a gold nanostar. *Nano Lett.* **2007**, *7*, 729–732.
[26] Sanchez-Gaytan, B. L.; Swanglap, P.; Lamkin, T. J.; Hickey, R. J.; Fakhraai, Z.; Link, S.; Park, S. J. Spiky gold nanoshells: Synthesis and enhanced scattering properties. *J. Phys. Chem. C* **2012**, *116*, 10318–10324.
[27] Zhao, Y.; Sun, M. Z.; Ma, W.; Kuang, H.; Xu, C. L. Biological molecules-governed plasmonic nanoparticle dimers with tailored optical behaviors. *J. Phys. Chem. Lett.* **2017**, *8*, 5633–5642.
[28] Li, M.; Cushing, S. K.; Zhang, J. M.; Lankford, J.; Aguilar, Z. P.; Ma, D. L.; Wu, N. Q. Shape-dependent surface-enhanced Raman scattering in gold-Raman-probe-silica sandwiched nanoparticles for biocompatible applications. *Nanotechnology* **2012**, *23*, 115501.
[29] Barbosa, S.; Agrawal, A.; Rodríguez-Lorenzo, L.; Pastoriza-Santos, I.; Alvarez-Puebla, R. A.; Kornowski, A.; Weller, H.; Liz-Marzan, L. M. Tuning size and sensing properties in colloidal gold nanostars. *Langmuir* **2010**, *26*, 14943–14950.
[30] Li, M.; Cushing, S. K.; Zhang, J. M.; Suri, S.; Evans, R.; Petros, W. P.; Gibson, L. F.; Ma, D. L.; Liu, Y. X.; Wu, N. Q. Three-dimensional hierarchical plasmonic nano-architecture enhanced surface-enhanced Raman scattering immunosensor for cancer biomarker detection in blood plasma. *ACS Nano* **2013**, *7*, 4967–4976.
[31] Niu, W. X.; Chua, Y. A. A.; Zhang, W. Q.; Huang, H. J.; Lu, X. M. Highly symmetric gold nanostars: Crystallographic control and surface-enhanced Raman scattering property. *J. Am. Chem. Soc.* **2015**, *137*, 10460–10463.
[32] Li, A. K.; Tang, L. J.; Song, D.; Song, S. S.; Ma, W.; Xu, L. G.; Kuang, H.; Wu, X. L.; Liu, L. Q.; Chen, X.; Xu, C. L. A SERS-active sensor based on heterogeneous gold nanostar core-silver nanoparticle satellite assemblies for ultrasensitive detection of aflatoxinB1. *Nanoscale* **2016**, *8*, 1873–1878.
[33] Sekhon, J. S.; Verma, S. S. Refractive index sensitivity analysis of Ag, Au, and Cu nanoparticles. *Plasmonics* **2011**, *6*, 311–317.
[34] Ma, Y. Y.; Li, W. Y.; Cho, E. C.; Li, Z. Y.; Yu, T.; Zeng, J.; Xie, Z. X.; Xia, Y. N. Au@Ag core-shell nanocubes with finely tuned and well-controlled sizes, shell thicknesses, and optical properties. *ACS Nano* **2010**, *4*, 6725–6734.
[35] Samal, A. K.; Polavarapu, L.; Rodal-Cedeira, S.; Liz-Marzán, L. M.; Pérez-Juste, J.; Pastoriza-Santos, I. Size tunable Au@Ag core-shell nanoparticles: Synthesis and surface-enhanced Raman scattering properties. *Langmuir* **2013**, *29*, 15076–15082.
[36] Goodman, A. M.; Cao, Y.; Urban, C.; Neumann, O.; Ayala-Orozco, C.; Knight, M. W.; Joshi, A.; Nordlander, P.; Halas, N. J. The surprising *in vivo* instability of near-IR-absorbing hollow Au-Ag nanoshells. *ACS Nano* **2014**, *8*, 3222–3231.
[37] Zhou, H. J.; Kim, J. P.; Bahng, J. H.; Kotov, N. A.; Lee, J. Self-assembly mechanism of spiky magnetoplasmonic supraparticles. *Adv. Funct. Mater.* **2014**, *24*, 1439–1448.
[38] Huang, Z. L.; Lei, X.; Liu, Y.; Wang, Z. W.; Wang, X. J.; Wang, Z. M.; Mao, Q. H.; Meng, G. W. Tapered optical fiber probe assembled with plasmonic nanostructures for surface-enhanced Raman scattering application. *ACS Appl. Mater. Interfaces* **2015**, *7*, 17247–17254.
[39] Weaver, J. H.; Frederikse, H. P. R. Optical properties of selected elements. In *CRC Handbook of Chemistry and Physics*: *A Ready-Reference Book of Chemical and Physical Data*; 86th ed. Lide, D. R., Ed.; CRC Press: Boca Raton, 2005; pp 134–135.
[40] Zhao, L. B.; Huang, Y. F.; Wu, D. Y.; Ren, B. Surface-enhanced Raman spectroscopy and plasmon-assisted photocatalysis of p-aminothiophenol. *Acta Chim. Sin.* **2014**, *72*, 1125–1138.
[41] Le Ru, E. C.; Blackie, E.; Meyer, M.; Etchegoin, P. G. Surface enhanced Raman scattering enhancement factors: A comprehensive study. *J. Phys. Chem. C* **2007**, *111*, 13794–13803.
[42] Zhu, C. H.; Meng, G. W.; Zheng, P.; Huang, Q.; Li, Z. B.; Hu, X. Y.; Wang, X. J.; Huang, Z. L.; Li, F. D.; Wu, N. Q. A hierarchically ordered array of silver-nanorod bundles for surface-enhanced Raman scattering detection of phenolic pollutants. *Adv. Mater.* **2016**, *28*, 4871–4876.
[43] Ma, L. W.; Huang, Y.; Hou, M. J.; Xie, Z.; Zhang, Z. J. Silver nanorods wrapped with ultrathin Al_2O_3 layers exhibiting excellent SERS sensitivity and outstanding SERS stability. *Sci. Rep.* **2015**, *5*, 12890.